


Exploration of the bright and dark exciton landscape and fine structure of MoS<sub>2</sub> using G<sub>0</sub>W<sub>0</sub>-BSEHongyu Yu,<sup>1,2</sup> Magdalena Laurien,<sup>1,\*</sup> Zhenpeng Hu,<sup>2</sup> and Oleg Rubel<sup>1,†</sup><sup>1</sup>*Department of Materials Science and Engineering, McMaster University, 1280 Main Street West, Hamilton, Ontario L8S 4L7, Canada*<sup>2</sup>*School of Physics, Nankai University, Tianjin 300071, China* (Received 17 April 2019; revised manuscript received 20 August 2019; published 10 September 2019)

Spectral ordering between dark and bright excitons in transition-metal dichalcogenides is of increasing interest for optoelectronic applications. However, little is known about dark exciton energies and their binding energies. We report the exciton landscape including momentum-forbidden dark excitons of the MoS<sub>2</sub> monolayer using single-shot GW–Bethe Salpeter equation (G<sub>0</sub>W<sub>0</sub>-BSE) calculations. We find the lowest-energy exciton to be indirect at ( $K'_v \rightarrow K_c$ ), in agreement with recent GdW-BSE calculations [T. Deilmann and K. S. Thygesen, *2D Mater.* **6**, 035003 (2019)]. We also find that by and large, the lowest-energy dark exciton binding energies ( $E_b$ ) scale with the quasiparticle energies ( $E_g$ ) according to the empirical  $E_b/E_g = 0.25$  rule. Differences in exciton binding energies are explained using an orbital theory.

DOI: 10.1103/PhysRevB.100.125413

## I. INTRODUCTION

Two-dimensional (2D) transition-metal dichalcogenides (TMDCs) like monolayer (ML) MoS<sub>2</sub> exhibit an intricate electronic fine structure that offers an abundance of possibilities to manipulate their optical and electrical properties and exploit them for novel devices. A fascinating aspect of ML materials that sets them apart from their bulk equivalents is the behavior of excitations: Quasiparticles formed by an excited electron and a hole (exciton) experience a greater Coulomb attraction in a monolayer material because of the lack of screening in the third dimension. These excitonic effects dominate the optical response of ML TMDCs.

Excitons can be either bright (optically accessible) or dark (optically inaccessible). Dark excitons can be classified according to two main characteristics: spin and location in the momentum space of the electron and hole. Spin-forbidden dark excitons are quasiparticles where the electron and the hole occupy the same position in momentum space, however, their spin is opposite and thus radiative recombination is not possible. Momentum-forbidden dark excitons consist of an electron and a hole located at different points in momentum space. Unassisted recombination is not possible for these indirect excitons either, thus they are dark.

Besides the bright states, dark excitons have a considerable influence on the optical response of TMDC MLs [1]. For example, spectral closeness of dark excitons to bright excitons can cause a significant drop in the photoluminescent yield in ML MoS<sub>2</sub> [2]. Similarly, higher-energy momentum-forbidden dark excitons can serve as a reservoir of charge carriers for bright transitions that are lower in energy and thus enhance the response for TMDC MLs [3]. Indirect excitons have also been related to the achievable degree of circular polarization in TMDC MLs [4] and the formation of quantum dots in

bilayer WSe<sub>2</sub> [5]. In addition, dark excitons in WSe<sub>2</sub> can be activated or brightened, i.e., the photoluminescence intensity increases, in the presence of a magnetic field, which leads to the creation of bright excitons with long and tunable lifetimes [6,7]. Brightening can also be achieved by strain [8] or the adsorption of high-dipole molecules [9], allowing for completely new device concepts in the design of high-sensitivity sensors.

Knowledge of the spectral relation of dark and bright excitons is important to fully understand the optical response of monolayer TMDCs [1,10]. This is especially crucial for ML MoS<sub>2</sub>, for which the ordering of the lowest-energy bright and dark excitons is still being discussed [11–13]. The spectral ordering of bright and dark excitons depends mainly on the amount of band splitting caused by spin-orbit coupling as well as the difference between the exciton binding energies. Initially, emphasis was placed on studying direct excitons [14]. However, comprehensive quantitative studies of the excitonic landscape including indirect, finite-momentum excitons are scarce. Important contributions were made first by Malic *et al.* [15], who calculated the optical response of group-VI TMDCs. They emphasized the importance of excitonic corrections to the band structure that can lead to a change in the band character from direct to indirect or affect the ordering of bright and dark states. However, their results showed only qualitative trends. Berghäuser *et al.* [16] obtained the exciton landscape of monolayer MoS<sub>2</sub> and other group-VI TMDCs using pump-probe experiments and an empirically parameterized quantum model. According to their study, the lowest-energy state for ML MoS<sub>2</sub> is a dark (indirect) exciton with its hole located at  $\Gamma_v$  and the electron located at  $K'_c$  ( $\Gamma_v \rightarrow K'_c$ ). Very recently, Deilmann and Thygesen [17] reported calculations of the exciton landscape including indirect excitons in the GdW + Bethe–Salpeter equation (BSE) scheme, where the approximation  $dW = W - W_{\text{metal}}$  enables a higher computational efficiency [18]. They found the excitonic state of monolayer MoX<sub>2</sub> to be dark (indirect) and located at  $K_v \rightarrow K'_c$ .

\*laurienm@mcmaster.ca

†rubelo@mcmaster.ca

In this report, we use *ab initio* calculations [single-shot GW ( $G_0W_0$ ) + BSE beyond the Tamm-Dancoff approximation (TDA)] to explore the whole bright and dark excitonic landscape of ML MoS<sub>2</sub> to contribute to the ongoing discussion. According to our results, the exciton ground state is a dark indirect exciton at  $K_v \rightarrow K'_c$ . We show that the lowest-energy spin-forbidden and indirect excitons obey the universal relationship between exciton energy and exciton binding energy proposed for bright excitons in 2D ML materials [19]. We discuss the variations in the binding energies in the light of orbital theory. We also show that the relationship breaks down for higher-energy excitons.

## II. METHODS

### A. $G_0W_0$ + BSE calculations

We performed  $G_0W_0$ -BSE *ab initio* calculations. The procedure for GW-BSE calculations is as follows: In the GW step the electronic ground state previously obtained using density functional theory [20] is corrected for quasiparticle effects. This correction is obtained by solving for the self-energy, which includes the many-body exchange-correlation interactions in a single shot. In Hedin's method [21], the self-energy is approximated by the product of the one-particle Green's function  $G$  and the screened Coulomb potential  $W$ . The quasiparticle corrected energies and wave functions are used as input for the BSE, which describes interactions of electron-hole pairs and directly yields the optical excitation energies. The exciton wave function is constructed as an expansion in terms of quasiparticle wave functions, and then the BSE can be solved self-consistently as an eigenvalue problem. In most cases, it is sufficient to solve the BSE in the TDA [22–24]:

$$(E_{c\mathbf{k}+\mathbf{Q}} - E_{v\mathbf{k}})A_{v\mathbf{c}\mathbf{k}}^{(S,\mathbf{Q})} + \sum_{v'c'k'} K_{v\mathbf{c}\mathbf{k},v'c'k'}^{AA}(\mathbf{Q})A_{v'c'k'}^{(S,\mathbf{Q})} = \Omega^{(S,\mathbf{Q})}A_{v\mathbf{c}\mathbf{k}}^{(S,\mathbf{Q})}. \quad (1)$$

Here  $\Omega^{(S,\mathbf{Q})}$  is the exciton energy (eigenvalue),  $E_{v\mathbf{k}}$  ( $E_{c\mathbf{k}+\mathbf{Q}}$ ) are the energies of the valence band (conduction band) obtained in the GW step,  $A_{v\mathbf{c}\mathbf{k}}^{(S,\mathbf{Q})}$  are expansion coefficients for the exciton wave function, and  $K$  is the interaction kernel which contains all the electron-hole interactions. Details concerning the mathematical form of  $K$  are given by Leng *et al.* [24]. The index  $\mathbf{Q}$  denotes a momentum transfer by a certain  $\mathbf{Q}$  vector. Here, we went beyond the TDA, including resonant-antiresonant coupling ( $K^{AB}$ ,  $K^{BA}$ ) [24],

$$(E_{c\mathbf{k}+\mathbf{Q}} - E_{v\mathbf{k}})A_{v\mathbf{c}\mathbf{k}}^{(S,\mathbf{Q})} + \sum_{v'c'k'} K_{v\mathbf{c}\mathbf{k},v'c'k'}^{AA}(\mathbf{Q})A_{v'c'k'}^{(S,\mathbf{Q})} + \sum_{v'c'k'} K_{v\mathbf{c}\mathbf{k},v'c'k'}^{AB}(\mathbf{Q})B_{v'c'k'}^{(S,\mathbf{Q})} = \Omega^{(S,\mathbf{Q})}A_{v\mathbf{c}\mathbf{k}}^{(S,\mathbf{Q})},$$

$$(E_{c\mathbf{k}+\mathbf{Q}} - E_{v\mathbf{k}})B_{v\mathbf{c}\mathbf{k}}^{(S,\mathbf{Q})} + \sum_{v'c'k'} K_{v\mathbf{c}\mathbf{k},v'c'k'}^{BB}(\mathbf{Q})B_{v'c'k'}^{(S,\mathbf{Q})} + \sum_{v'c'k'} K_{v\mathbf{c}\mathbf{k},v'c'k'}^{BA}(\mathbf{Q})A_{v'c'k'}^{(S,\mathbf{Q})} = \Omega^{(S,\mathbf{Q})}B_{v\mathbf{c}\mathbf{k}}^{(S,\mathbf{Q})}, \quad (2)$$

where  $B_{v\mathbf{c}\mathbf{k}}^{(S,\mathbf{Q})}$  are expansion coefficients for the antiresonant part of the exciton wave function.

The main reason to conduct calculations beyond the TDA for our work was that the software used does not recommend the calculation of finite-momentum excitons within the TDA. The TDA has been shown to break down for nanoscale systems [25–27] and to deviate from experiment for finite-momentum excitons in silicon [28]. However, we do not expect the resonant-antiresonant coupling to have a great effect on the optical properties of an ML TMDC.

To the best of our knowledge, solving the BSE beyond the TDA has not yet been reported for group-VI transition-metal dichalcogenides. In the following we describe the details of our settings used to perform the  $G_0W_0$ -BSE beyond TDA calculations.

### B. Computational details

The calculations were performed with the Vienna *ab initio* package (VASP) [29,30], version 5.4.4. The projector-augmented wave method [31,32] was used to treat core and valence electrons, with 14 electrons for Mo and 6 electrons for S explicitly included in the valence states. The plane-wave energy cutoff was set to 400 eV. Recommended GW projector-augmented wave potentials supplied by VASP were employed for all atoms. The Perdew-Burke-Ernzerhof [33] exchange-correlation functional was used to obtain the electronic ground state with density functional theory [20,34]. To ensure minimal interlayer coupling, monolayers were separated by 21.5 Å of vacuum, which is sufficient for the longitudinal component of the macroscopic static dielectric tensor to be close to unity. Atomic positions and lattice vectors were fully relaxed with a tolerance of 0.01 eV/Å. Only the  $\mathbf{c}$  vector (out-of-plane vector) was fixed during the relaxation procedure. Electronic minimization was performed with a tolerance of  $10^{-7}$  eV and convergence accelerated with Gaussian smearing of the Fermi surface by 0.05 eV. The Brillouin zone was sampled with a  $12 \times 12 \times 1$   $\Gamma$ -centered  $k$ -point mesh in order to include high-symmetry points in the  $k$  mesh and ensure sufficient accuracy of the exciton binding energy, which is highly dependent on the density of the  $k$  mesh [35]. After structure relaxation, we obtained a lattice constant of 3.185 Å, a metal-chalcogen (M-X) bond length of 2.414 Å, and a chalcogen-chalcogen X-X bond length of 3.128 Å. The obtained lattice constant is close to the experimental lattice constant of bulk MoS<sub>2</sub> ( $a = 3.16$  Å) [36–38] and in excellent agreement with other computational studies [39–41]. The M-X bond length is in very good agreement with experimental data [42,43].

For all calculations following the relaxation procedure, we considered spin-orbit coupling and included 640 bands (26 of them occupied) in order to have enough empty bands for the ensuing GW calculations. Further, the orbitals were enforced to have real values at the  $\Gamma$  point and points at the edge of the Brillouin zone, and as a consequence the symmetry was turned off.

We calculated the quasiparticle band structure at the single-shot  $G_0W_0$  level of theory. For the response function we set a cutoff of 250 eV; this parameter controls how many  $\mathbf{G}$  vectors are included in the GW calculation. The number of frequency grid points was set to 96. For visualizing the quasiparticle

band structure we applied Wannier interpolation using the WANNIER90 program [44].

The BSE calculations were carried out beyond the Tamm-Dancoff approximation using the full BSE Hamiltonian [28], which means that resonant-antiresonant coupling is included. For solving the BSE, we considered six occupied bands and eight virtual (unoccupied) bands of the quasiparticle band structure as a basis for excitonic eigenstates. To obtain finite-momentum excitons, we iterated over all possible  $\mathbf{Q}$  vectors that could be selected for the given  $k$  mesh in the first Brillouin zone (144 in total) and additional  $\mathbf{Q}$  vectors outside the first Brillouin zone to include the  $K'_v \rightarrow K_c$ ,  $K_v \rightarrow K'_c$ , and  $K'_v \rightarrow \Lambda_c$  transitions. For all  $\mathbf{Q}$  vectors, we obtained the lowest 100 eigenstates as output. We chose the  $k$  point with the biggest contribution to the exciton wave function (highest amplitude) for each eigenstate as the momentum vector of the hole of the exciton. Exciton binding energies were calculated by subtracting the BSE eigenvalues from the GW band gap matching the position of the hole and electron of the exciton in momentum space. To distinguish between spin-parallel and spin-antiparallel states, the spinor up and down components ( $\alpha$  and  $\beta$ ) were determined from spin projections as described in Refs. [45,46].

We would like to point out certain limitations of our methods. The  $G_0W_0$ -BSE procedure as implemented in VASP and as used for this work does not provide the option to truncate the Coulomb interaction between periodic images. Carefully conducted studies [47,48] show that Coulomb truncation is essential for achieving convergence of the GW band energy corrections, as without the truncation the periodic images of the monolayer increase the dielectric function, especially in the low- $\mathbf{Q}$  limit. Further, a very high- $k$  mesh, up to  $300 \times 300 \times 1$ , is required in order to converge the exciton binding energy to within 0.1 eV [48]. As our  $G_0W_0$  calculations and the BSE beyond TDA calculations were conducted without considering geometrical and time-reversal symmetries, the computational cost precludes the use of fine  $k$  meshes (due to excessive memory requirements). However, the errors of not truncating the Coulomb interaction and using a coarse  $k$  mesh partly cancel out [47].

We conducted convergence tests that suggest that the total error of the quasiparticle band gap is below 0.1 eV and the variation of the spectral spacing with  $k$  grid density is about one order of magnitude smaller than the actual energy spacing [49].

### III. RESULTS AND DISCUSSION

We first discuss the effect of including the resonant-antiresonant coupling (going beyond the TDA). The TDA affects only the BSE step of the calculations. We performed a comparative BSE calculation employing the TDA to investigate the effects of the absence of resonant-antiresonant coupling on the optical properties of ML MoS<sub>2</sub>. The results are identical to the full BSE calculations; differences are negligible. This is true for the spectral spacing of the excitons [50] as well as for the dielectric response (data not shown).

Now we turn to the results of the main calculations. The quasiparticle band structure of monolayer MoS<sub>2</sub> is shown in Fig. 1. The bands are obtained by Wannier interpolation of

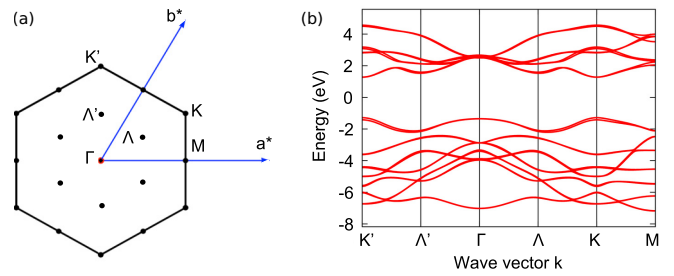


FIG. 1. (a) First Brillouin zone of monolayer MoS<sub>2</sub> and (b) quasiparticle band structure after Wannier interpolation. The direct band gap is located at  $K$  ( $K'$ ).

the GW eigenvalues. The band structure shows a direct band gap of ca. 2.43 eV at the  $K$  and  $K'$  points. These points are equivalent (except for their spin) because of the time-reversal symmetry. Besides  $K$  and  $K'$ ,  $\Lambda$  and  $\Lambda'$  are related via time-reversal symmetry. For future discussion we refer to only one of the transitions related via time-reversal symmetry.

The optical response of TMDC monolayers is dominated by the presence of excitons and their binding energies. As a result, the optical energy gap is much smaller than the quasiparticle band gap. This can be seen when considering the absorption spectrum of ML MoS<sub>2</sub> for the direct transitions ( $\mathbf{Q} = 0$ ) obtained from our BSE calculations [Fig. 2(a)]. The A and B excitons are located at ca. 1.8 and 1.95 eV, implying binding energies of about 0.62 and 0.48 eV, respectively. The spin-forbidden dark exciton is slightly lower in energy than the bright exciton. The absorption spectrum is in good

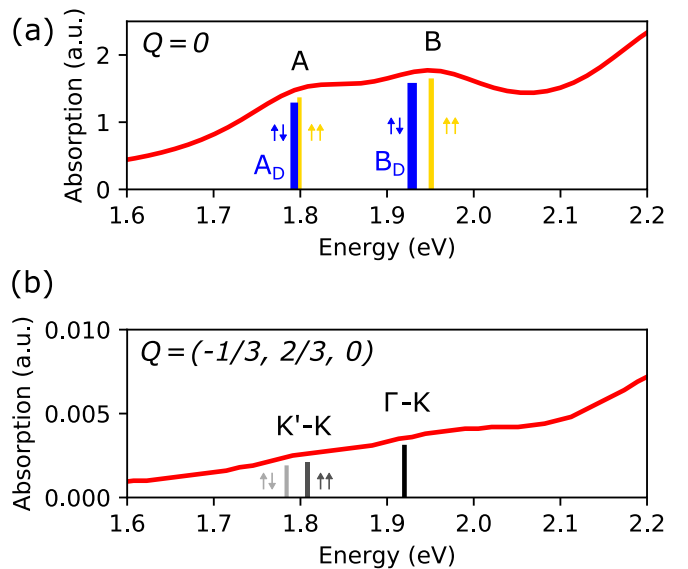


FIG. 2. Absorption spectra of MoS<sub>2</sub>. Shown is the imaginary part of the dielectric function obtained from the BSE calculation. (a)  $\mathbf{Q} = 0$  denotes the absorption spectrum of the direct transitions. The first two absorption peaks denote the A and B excitons located at the  $K$  point. The dark (spin-forbidden) exciton is lower in energy than the bright exciton for both A and B excitons. (b)  $\mathbf{Q} = (-1/3, 2/3, 0)$  captures the the  $K'_v \rightarrow K_c$  and  $\Gamma_v \rightarrow K'_c$  transitions. The indirect exciton at  $K'_v \rightarrow K_c$  is clearly lower in energy than the dark direct exciton at  $K$ .

qualitative agreement with experiments [51,52] as well as other theoretical studies [53,54]. The energies of the A and B peaks are blue-shifted in comparison to experiment. This comes about for two reasons; missing substrate effects [55] as well as  $k$ -grid-dependent binding energies. The denser the  $k$  grid, the lower (i.e., better converged) the binding energies become [35,56].

The values obtained from our calculations for the band gap and exciton binding energies are in good agreement with experiment. Using scanning tunneling spectroscopy and optical reflectance contrast measurements for MoS<sub>2</sub> on fused silica, Rigosi *et al.* [57] obtained a binding energy of the bright excitons of  $0.31 \pm 0.04$  eV and an electronic band gap of  $2.17 \pm 0.1$  eV. The results of our calculation with  $E_b = 0.624$  eV and  $E_g = 2.42$  eV are slightly higher than the experimental values because the calculations are obtained for a free-standing monolayer and a relatively coarse  $k$  mesh. Other computational studies using GW-BSE found results that are quite close to ours, obtaining 2.42 eV for the band gap and 0.57 eV for the bright exciton binding energy [19]. The difference in the  $E_b$  can be explained by the  $k$ -mesh density: Jiang *et al.* [19] used a  $k$  mesh of  $16 \times 16 \times 1$  (our calculations:  $12 \times 12 \times 1$ ) and the binding energy strongly depends on the  $k$  mesh [35]. For example, in our convergence calculations for the lowest-energy direct exciton at the  $K$  point, we found an exciton binding energy of 0.551 eV for a  $k$  grid of  $15 \times 15 \times 1$  and the nearly twice as high binding energy of 1.061 eV for a  $k$  grid of  $6 \times 6 \times 1$  [56].

Figure 2(b) shows the spectra for indirect excitons with a  $\mathbf{Q}$  vector of  $(-1/3, 2/3, 0)$ . This  $\mathbf{Q}$  vector captures the the  $K'_v \rightarrow K_c$  and  $\Gamma_v \rightarrow K'_c$  transitions. It becomes clear that there exists a lower-energy exciton that is indirect at  $K'_v \rightarrow K_c$  with an exciton energy of less than 1.8 eV.

To capture the effect of all important indirect excitons on the quasiparticle band structure, we plot the exciton band structure in a 2D fashion. This allows us to show the renormalization of the eigenvalues caused by direct, indirect, and dark excitons at the same time. In Fig. 3 the landscape of bright and dark excitons in ML MoS<sub>2</sub> is shown for the most important points in momentum space. To accommodate momentum-forbidden dark excitons, the  $k$  vectors of the electron and hole of an exciton are displayed separately on the two axes of the graph. Further, we distinguish between spin-up and spin-down states to allow for the visualization of spin-forbidden excitons. As a result, bright excitons are seen on the dashed red diagonal line, spin-forbidden direct excitons on the dotted blue line, and momentum-forbidden excitons are located to the sides. Also, spin-allowed excitons are distributed in the lower half of the plot, while spin-forbidden excitons are placed in the upper half. Each circle represents an exciton; the color displays the exciton energy and the radius of the circle corresponds to the exciton binding energy. The symmetry of the wave function  $\Phi$  of the exciton can be expressed as

$$\Phi(\mathbf{k}_h, \mathbf{k}_e, \mathbf{s}_h, \mathbf{s}_e) = \Phi^*(-\mathbf{k}_h, -\mathbf{k}_e, -\mathbf{s}_h, -\mathbf{s}_e). \quad (3)$$

As a result, excitons  $|\mathbf{k}_h, \mathbf{k}_e, \mathbf{s}_h, \mathbf{s}_e\rangle$  and  $|-\mathbf{k}_h, -\mathbf{k}_e, -\mathbf{s}_h, -\mathbf{s}_e\rangle$  should have the same properties. As necessitated by our procedure, we calculated the whole Brillouin zone irrespective of time-reversal symmetry. Because of this, our results showed computational inaccuracies in the single-digit meV range for

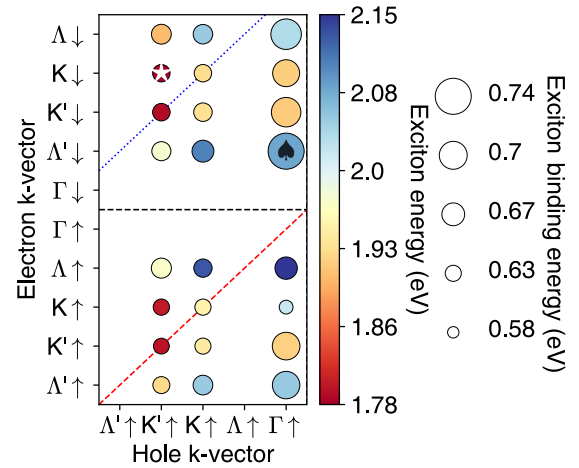


FIG. 3. MoS<sub>2</sub> exciton landscape including dark and bright excitons. The color scale reflects the exciton energy and the circle size represents the exciton binding energy. In order to display finite-momentum excitons, hole and electron  $k$  vectors are displayed separately on the horizontal and vertical axes, respectively. The lowest-energy exciton (star) is located at  $K'_v \uparrow \rightarrow K_c \downarrow$  and is therefore momentum forbidden. The highest binding energy (spade) occurs for an indirect exciton at  $\Gamma_v \uparrow \rightarrow \Lambda'_c \downarrow$ .

the band energies (and the  $K$ -point exciton energies) between identical states related by the time-reversal symmetry. The energy values presented here are always chosen from the exciton with the lower energy of the two (by time-reversal symmetry) identical states. Due to time-reversal symmetry we show only one half of the hole states in Fig. 3. The other half would be equal to the first by center symmetry. Although unoccupied, we chose to include the  $\Lambda_v$  and the  $\Gamma_c$  states to preserve the center symmetry.

The exciton with the highest binding energy of 0.712 eV (shown by a spade) is located at  $\Gamma_v \uparrow$  (hole) and  $\Lambda'_c \downarrow$  (electron) ( $\Gamma_v \uparrow \rightarrow \Lambda'_c \downarrow$ ). The lowest-energy exciton (shown by a star) has an energy of 1.784 eV and is located at  $K'_v \uparrow \rightarrow K_c \downarrow$ . This implies that after considering excitonic effects, we find a change in the optical band gap location of MoS<sub>2</sub> with regard to the transport band gap: the optical band gap is now indirect. The exciton at  $K'_v \uparrow \rightarrow K_c \downarrow$  is 15 meV lower in energy than the bright exciton at  $K$  and 9 meV lower in energy than the spin-forbidden direct exciton at  $K$ . The band ordering is illustrated in Fig. 4.

Besides the evaluation of the spin states, dark and bright excitons can be distinguished by their oscillator strengths. The oscillator strength of bright excitons is several magnitudes higher than that of dark excitons [12]. In Fig. 5 we show the oscillator strength (circle size) obtained by solving the BSE paired with the quasiparticle band gap (color map) in a similar fashion to the exciton landscape. We find that the direct, spin-allowed excitons at  $K$  and  $K'$  are about 1400 times higher in oscillator strength than their spin-forbidden equivalents.

Figure 5 also shows that our GW calculations predict a direct band gap at  $K$  with the valence and conduction bands having the same spin. The lower-energy spin-forbidden excited state after considering excitonic effects arises due to different exciton binding energies ( $E_b$ ) of the dark and the

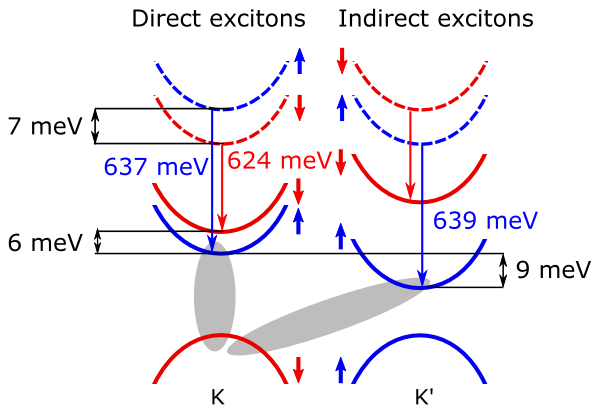


FIG. 4. Schematic of the lowest-energy excitons at the  $K$ - $K'$  valley of ML  $\text{MoS}_2$ . The ordering of solid energy bands corresponds to the exciton-corrected energies. The dashed conduction bands denote the quasiparticle band ordering. The lowest-energy exciton is indirect and located at  $K$ - $K'$ . The lowest direct exciton is located at  $K$  and spin forbidden (shaded area). This result is linked to spin-orbit coupling and the differences in the exciton binding energies, which are higher for the spin- and momentum-forbidden excitons than for the bright exciton (637, 639, and 624 meV, respectively).

bright excitons: The  $E_b$  of the indirect dark exciton ( $E_b = 0.637$  eV) is about 13 meV higher than the binding energy of the bright exciton ( $E_b = 0.624$  eV), while the spin splitting of the conduction band is only about 7 meV (see Fig. 4). Thus, after consideration of excitonic effects, the spin transition at  $K$  is lower in energy than the spin-allowed transition. These results are in agreement with those of Qiu *et al.* [11] and Deilmann and Thygesen [17], who also found that the dark exciton at  $K$  is lower in energy than the bright exciton. Echeverry *et al.* [12], using the GW-BSE method, came to the opposite conclusion. Qiu *et al.* [48] attribute the differing

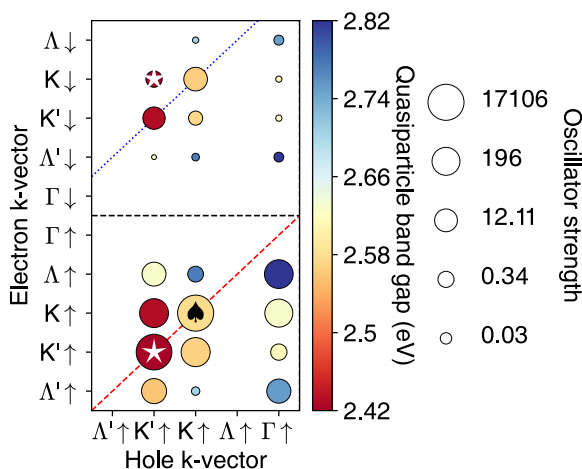


FIG. 5.  $\text{MoS}_2$  quasiparticle band gaps (color scale) and oscillator strengths (open white circles at right on a log scale) for bright and dark excitons. The quasiparticle band gap (star) is located at  $K' \uparrow$  ( $K \downarrow$ ). An indirect band gap of equal energy is located at  $K'_v \uparrow$ - $K_c \downarrow$ . The oscillator strength of the bright transitions is several magnitudes higher than that of the dark transitions; the highest oscillator strength corresponds to the  $K'_v \uparrow \rightarrow K'_c \uparrow$  transition (spade).

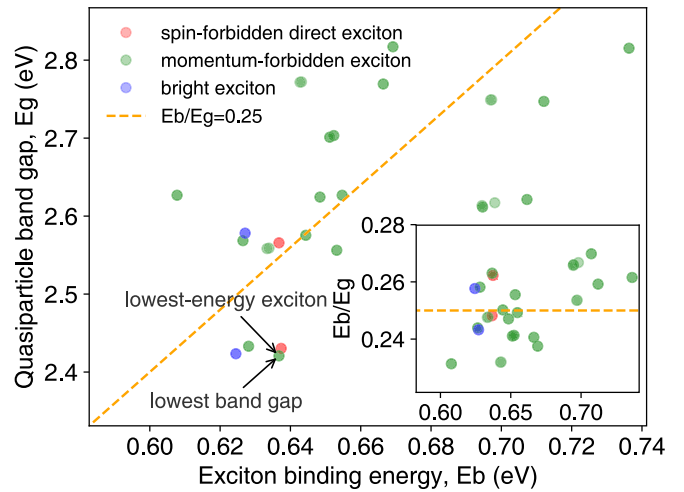


FIG. 6. Ratio of the exciton binding energy ( $E_b$ ) to the quasiparticle band gap ( $E_g$ ) for  $\text{MoS}_2$ . Bright excitons (blue circles), spin-forbidden excitons (red circles), and momentum-forbidden excitons (green circles) are shown. The relationship  $E_b/E_g = 0.25$  according to Jiang *et al.* [19] is shown by the dashed line. Inset: The ratio  $E_b/E_g$  over  $E_b$ . All excitons are contained in the  $E_b/E_g$  range 0.23–0.28 and thus are not too far from the 0.25 rule.

results in the literature to different settings of the density functional theory, GW, and BSE parameters.

Now we discuss the binding energies of the whole exciton landscape in more detail. Most of the holes of the excitons are located at  $\Gamma$  or  $K$  and the electrons of the excitons are located at  $\Lambda$  or  $K$  (see Fig. 3). Interestingly, the exciton binding energy of excitons whose hole is at  $\Gamma$  is almost always higher than that of excitons whose hole is located at  $K$ . For bulk semiconductors this effect could be explained by the effective mass differences, as holes at the  $\Gamma$  point are heavier than holes at the  $K$  point [58]. However, for the binding energies of 2D materials the effective mass does not play a significant role, provided the polarizability is large (which is the case for  $\text{MoS}_2$ ) [19,58].

Further, it is well known that the high binding energy of 2D materials originates from the lack of screening in the third dimension. Hence, we expect one factor for the different binding energies to be differences in screening depending on the position of the electron in real space. To qualitatively compare the amount of screening experienced by different excitons, we performed an orbital analysis for the valence and conduction band states of each exciton. The basic idea is that electrons occupying orbitals pointing perpendicular to the layer experience less screening than electrons of orbitals confined within the plane of the monolayer. By convention,  $z$  is taken as the out-of-plane axis. It is well known that for monolayer  $\text{MoS}_2$ ,  $\Gamma_v$  exhibits high contributions of the  $\text{Mo-}d_{z^2}$  and  $\text{S-}p_z$  orbitals, while the  $K_v$  state is mainly composed of  $d_{xy}$  orbitals [42]. For our calculations we find the  $\Gamma_v$  state to consist of ca. 77%  $d_{z^2} + 22\%$   $p_z$  and the  $K_v$  state of 41%  $d_{xy} + 41\%$   $d_{x^2-y^2}$ . Thus we can expect excitons at  $\Gamma_v$  to experience less screening and consequently have higher binding energies than excitons at  $K_v$ .

Figure 6 shows the relationship between the quasiparticle band gap and the exciton binding energy, including the

lowest-energy bright, spin-forbidden, and momentum-forbidden excitons. Generally, excitons at large quasiparticle band gaps have higher exciton binding energies. We include a dashed line in the figure that represents the  $E_b/E_g = 0.25$  rule for excitons of 2D materials proposed by Jiang *et al.* [19]. Momentum-allowed excitons follow the rule that the exciton binding energy is about 0.25 of the quasiparticle band gap [19] irrespective of their spin. Momentum-forbidden excitons also generally follow the trend of the exciton binding energy being about 0.25 of the band gap, but with more scattering (ratios from 0.23 to 0.28). The inset in Fig. 6 shows a trend toward indirect excitons: the higher the binding energy  $E_b$ , the higher is the ratio  $E_b/E_g$ . What causes this relationship?

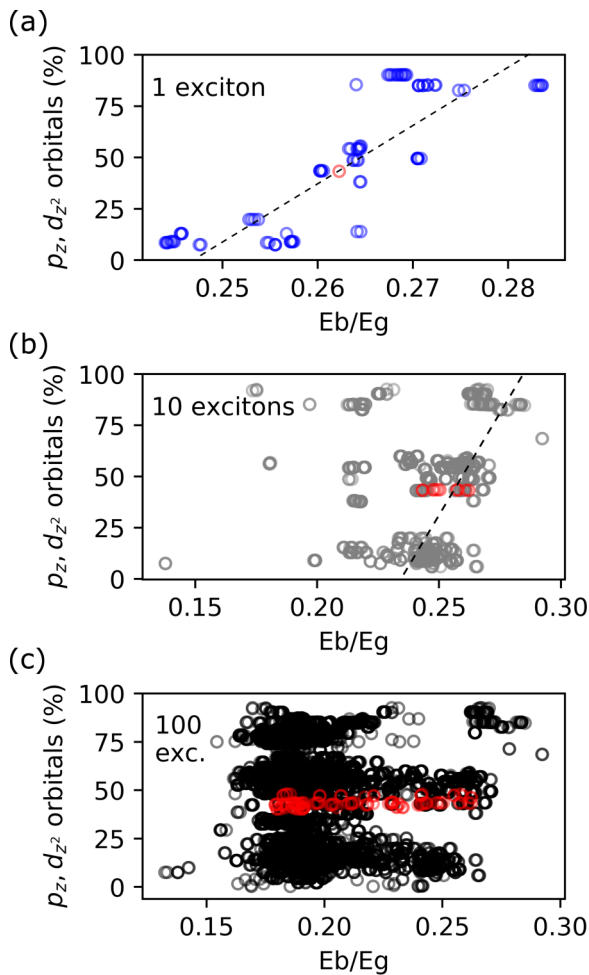


FIG. 7. Orbital contributions to valence and conduction band states of indirect excitons in MoS<sub>2</sub> over the ratio of the exciton binding energy ( $E_b$ ) and quasiparticle band gap ( $E_g$ ) for MoS<sub>2</sub>. Direct excitons are also shown (red circles). (a) For the lowest-energy excitons (1 exciton per  $\mathbf{Q}$  vector) there is a clear dependence of the  $E_b/E_g$  ratio on the contributions of the  $p_z$  and  $d_{z^2}$  orbitals (the dashed line is included as a guide for the eye). (b, c) The more higher-energy excitons are included for each  $\mathbf{Q}$  vector, the less obvious this dependence becomes, and it finally vanishes (10 and 100 lowest-energy excitons). At higher energies, exciton charge carriers are screened and the hole and electron progressively behave as free charge carriers causing the binding energy to decrease.

In order to explore this in more detail we next consider the exciton landscape including higher-energy excitons, up to 100 per  $\mathbf{Q}$  vector, and their orbital compositions. We determined the  $d_{z^2}$ - and  $p_z$ -orbital contributions of the hole and electron states of each exciton and plotted the sum of them versus the  $E_b/E_g$  ratio (Fig. 7). For the lowest-energy excitons, excitons with higher  $E_b/E_g$  ratios show a higher percentage of  $d_{z^2}$  and  $p_z$  orbitals. In other words, there exists a correlation between the  $E_b/E_g$  ratio and the orbital contributions. This result explains the range of the  $E_b/E_g$  ratio shown in Fig. 6. It can also be seen that the direct excitons (red circles in Fig. 7) are confined to a narrow region of  $d_{z^2}$  and  $p_z$  percentages, just below 50%. As a result, the  $E_b/E_g$  ratio does not scatter as much for the direct lowest-energy excitons as for the indirect excitons. However, upon the inclusion of higher-energy excitons, the  $E_b/E_g = 0.25$  relationship completely breaks down; the  $E_b/E_g$  ratio also becomes largely independent of the orbital composition. The relationship of binding energy and orbital contributions becomes less clear and vanishes when the 100 lowest-energy excitons for each  $\mathbf{Q}$  vector are included. We attribute this to the weaker electron-hole interactions for excitons with higher energies. At these energies, excitons are closely spaced and decrease rapidly in binding energy, behaving as uncorrelated electron-hole pairs [54]. The decrease in the  $E_b/E_g$  ratio with quasiparticle energy is shown in the Supplemental Material [59].

#### IV. CONCLUSION

In conclusion, we perform calculations of finite-momentum excitons in MoS<sub>2</sub> monolayers within and beyond the first Brillouin zone. It is found that the holes of the lowest-energy excitons are located at the  $\Gamma$  or  $K$  valleys, while the electrons reside in the  $K$  or  $\Lambda$  valleys. Our calculations predict the lowest-energy exciton to be indirect at  $K - K'$ , which is in agreement with recent GdW-BSE calculations [17]. The energy difference between the indirect exciton at  $K - K'$  and the spin-forbidden direct exciton at  $K - K$  is about 9 meV. The bright exciton is located at  $K$  and 15 meV higher in energy than the lowest-energy exciton at  $K - K'$ . We also discuss the exciton binding energies. The ratio  $E_b/E_g = 0.25$  found for bright excitons in 2D monolayer materials holds true approximately for dark and indirect excitons. Excitons contained in orbitals that point out of plane and thus experience less local screening show higher binding energies. The relation of exciton binding energies to the orbital composition and the  $E_b/E_g = 0.25$  relation both break down for higher-energy excitons.

#### ACKNOWLEDGMENTS

H.Y. acknowledges support from the National Science Fund of China for Talent Training in the Basic Sciences (Grant No. J1103208). M.L. and O.R. acknowledge funding provided by the Natural Sciences and Engineering Research Council of Canada under the Discovery Grant Programs (Grant No. RGPIN-2015-04518). Calculations were performed using a Compute Canada infrastructure supported by the Canada Foundation for Innovation under the John R. Evans Leaders Fund.

H.Y. and M.L. contributed equally to this work.

- [1] T. Mueller and E. Malic, *npj 2D Mater. Appl.* **2**, 29 (2018).
- [2] F. Wu, F. Qu, and A. H. MacDonald, *Phys. Rev. B* **91**, 075310 (2015).
- [3] A. Steinhoff, M. Florian, M. Rösner, G. Schönhoff, T. Wehling, and F. Jahnke, *Nat. Commun.* **8**, 1166 (2017).
- [4] M. Baranowski, A. Surrente, D. K. Maude, M. Ballottin, A. A. Mitoglu, P. C. M. Christianen, Y. C. Kung, D. Dumcenco, A. Kis, and P. Plochocka, *2D Mater.* **4**, 025016 (2017).
- [5] J. Lindlau, M. Selig, A. Neumann, L. Colombier, J. Förste, V. Funk, M. Förg, J. Kim, G. Berghäuser, T. Taniguchi *et al.*, *Nat. Commun.* **9**, 2586 (2018).
- [6] X.-X. Zhang, T. Cao, Z. Lu, Y.-C. Lin, F. Zhang, Y. Wang, Z. Li, J. C. Hone, J. A. Robinson, D. Smirnov *et al.*, *Nat. Nanotechnol.* **12**, 883 (2017).
- [7] R. Vasconcelos, H. Bragança, F. Qu, and J. Fu, *Phys. Rev. B* **98**, 195302 (2018).
- [8] M. Feierabend, Z. Khatibi, G. Berghäuser, and E. Malic, *Phys. Rev. B* **99**, 195454 (2019).
- [9] M. Feierabend, G. Berghäuser, A. Knorr, and E. Malic, *Nat. Commun.* **8**, 14776 (2017).
- [10] M. Selig, G. Berghäuser, M. Richter, R. Bratschitsch, A. Knorr, and E. Malic, *2D Mater.* **5**, 035017 (2018).
- [11] D. Y. Qiu, F. H. da Jornada, and S. G. Louie, *Phys. Rev. Lett.* **111**, 216805 (2013).
- [12] J. P. Echeverry, B. Urbaszek, T. Amand, X. Marie, and I. C. Gerber, *Phys. Rev. B* **93**, 121107(R) (2016).
- [13] M. Molas, C. Faugeras, A. Slobodeniuk, K. Nogajewski, M. Bartos, D. Basko, and M. Potemski, *2D Mater.* **4**, 021003 (2017).
- [14] G. Wang, A. Chernikov, M. M. Glazov, T. F. Heinz, X. Marie, T. Amand, and B. Urbaszek, *Rev. Mod. Phys.* **90**, 021001 (2018).
- [15] E. Malic, M. Selig, M. Feierabend, S. Brem, D. Christiansen, F. Wendler, A. Knorr, and G. Berghäuser, *Phys. Rev. Mater.* **2**, 014002 (2018).
- [16] G. Berghäuser, P. Steinleitner, P. Merkl, R. Huber, A. Knorr, and E. Malic, *Phys. Rev. B* **98**, 020301(R) (2018).
- [17] T. Deilmann and K. S. Thygesen, *2D Mater.* **6**, 035003 (2019).
- [18] M. Drüppel, T. Deilmann, J. Noky, P. Maruhn, P. Krüger, and M. Rohlfing, *Phys. Rev. B* **98**, 155433 (2018).
- [19] Z. Jiang, Z. Liu, Y. Li, and W. Duan, *Phys. Rev. Lett.* **118**, 266401 (2017).
- [20] W. Kohn and L. J. Sham, *Phys. Rev.* **140**, A1133 (1965).
- [21] L. Hedin, *Phys. Rev.* **139**, A796 (1965).
- [22] I. Tamm, in *Selected Papers* (Springer, Berlin, 1991), pp. 157–174.
- [23] S. M. Dancoff, *Phys. Rev.* **78**, 382 (1950).
- [24] X. Leng, F. Jin, M. Wei, and Y. Ma, *WIREs Comput. Mol. Sci.* **6**, 532 (2016).
- [25] Y. Ma, M. Rohlfing, and C. Molteni, *Phys. Rev. B* **80**, 241405(R) (2009).
- [26] P. Puschnig, C. Meisenbichler, and C. Draxl, *arXiv:1306.3790*.
- [27] M. Gruning, A. Marini, and X. Gonze, *Nano Lett.* **9**, 2820 (2009).
- [28] T. Sander, E. Maggio, and G. Kresse, *Phys. Rev. B* **92**, 045209 (2015).
- [29] G. Kresse and J. Hafner, *Phys. Rev. B* **47**, 558 (1993).
- [30] G. Kresse and J. Furthmüller, *Comp. Mater. Sci.* **6**, 15 (1996).
- [31] P. E. Blöchl, *Phys. Rev. B* **50**, 17953 (1994).
- [32] G. Kresse and D. Joubert, *Phys. Rev. B* **59**, 1758 (1999).
- [33] J. P. Perdew, K. Burke, and M. Ernzerhof, *Phys. Rev. Lett.* **77**, 3865 (1996).
- [34] P. Hohenberg and W. Kohn, *Phys. Rev.* **136**, B864 (1964).
- [35] M. Bokdam, T. Sander, A. Stroppa, S. Picozzi, D. D. Sarma, C. Franchini, and G. Kresse, *Sci. Rep.* **6**, 28618 (2016).
- [36] K. Bronsema, J. De Boer, and F. Jellinek, *Z. Anorg. Allg. Chem.* **540**, 15 (1986).
- [37] B. Schönfeld, J. Huang, and S. Moss, *Acta Crystallogr. Sec. B: Struct. Sci* **39**, 404 (1983).
- [38] J. Wildervanck and F. Jellinek, *Z. Anorg. Allg. Chem.* **328**, 309 (1964).
- [39] J. Kang, S. Tongay, J. Zhou, J. Li, and J. Wu, *Appl. Phys. Lett.* **102**, 012111 (2013).
- [40] G.-B. Liu, W.-Y. Shan, Y. Yao, W. Yao, and D. Xiao, *Phys. Rev. B* **88**, 085433 (2013).
- [41] A. Ramasubramaniam, *Phys. Rev. B* **86**, 115409 (2012).
- [42] M. Samadi, N. Sarikhani, M. Zirak, H. Zhang, H.-L. Zhang, and A. Z. Moshfegh, *Nanoscale Horiz.* **3**, 90 (2018).
- [43] R. G. Dickinson and L. Pauling, *J. Am. Chem. Soc.* **45**, 1466 (1923).
- [44] A. A. Mostofi, J. R. Yates, Y.-S. Lee, I. Souza, D. Vanderbilt, and N. Marzari, *Comput. Phys. Commun.* **178**, 685 (2008).
- [45] F. Giustino, *Materials Modelling Using Density Functional Theory: Properties and Predictions* (Oxford University Press, Oxford, UK, 2014).
- [46] C. Zheng, S. Yu, and O. Rubel, *Phys. Rev. Mater.* **2**, 114604 (2018).
- [47] F. Hüser, T. Olsen, and K. S. Thygesen, *Phys. Rev. B* **88**, 245309 (2013).
- [48] D. Y. Qiu, F. H. da Jornada, and S. G. Louie, *Phys. Rev. B* **93**, 235435 (2016).
- [49] See Supplemental Material at <http://link.aps.org/supplemental/10.1103/PhysRevB.100.125413> for convergence tests.
- [50] See Supplemental Material at <http://link.aps.org/supplemental/10.1103/PhysRevB.100.125413> for a comparison of TDA and full BSE results on the spectral spacing of excitons [Fig. S2(b)].
- [51] K. F. Mak, C. Lee, J. Hone, J. Shan, and T. F. Heinz, *Phys. Rev. Lett.* **105**, 136805 (2010).
- [52] K. P. Dhakal, D. L. Duong, J. Lee, H. Nam, M. Kim, M. Kan, Y. H. Lee, and J. Kim, *Nanoscale* **6**, 13028 (2014).
- [53] M. Palummo, M. Bernardi, and J. C. Grossman, *Nano Lett.* **15**, 2794 (2015).
- [54] M. Bernardi, C. Ataca, M. Palummo, and J. C. Grossman, *Nanophotonics* **6**, 479 (2017).
- [55] B. Mukherjee, F. Tseng, D. Gunlycke, K. K. Amara, G. Eda, and E. Simsek, *Opt. Mater. Express* **5**, 447 (2015).
- [56] See Supplemental Material at <http://link.aps.org/supplemental/10.1103/PhysRevB.100.125413> for the dependence of exciton binding energies on the  $k$  grid (Table S1).
- [57] A. F. Rigosi, H. M. Hill, K. T. Rim, G. W. Flynn, and T. F. Heinz, *Phys. Rev. B* **94**, 075440 (2016).
- [58] T. Olsen, S. Latini, F. Rasmussen, and K. S. Thygesen, *Phys. Rev. Lett.* **116**, 056401 (2016).
- [59] See Supplemental Material at <http://link.aps.org/supplemental/10.1103/PhysRevB.100.125413> for the decrease in the  $E_b/E_g$  ratio with the quasiparticle energy (Fig. S3).

## Supplementary material for:

# Exploration of the bright and dark exciton landscape and fine structure of MoS<sub>2</sub> (using G<sub>0</sub>W<sub>0</sub>-BSE)

Hongyu Yu,<sup>1,2</sup> M. Laurien,<sup>1\*</sup> Zhenpeng Hu,<sup>2</sup> and O. Rubel<sup>1†</sup>

<sup>1</sup>*Department of Materials Science and Engineering, McMaster University, 1280 Main Street West, Hamilton, Ontario L8S 4L7, Canada*

<sup>2</sup>*School of Physics, Nankai University, Tianjin 300071, China*

### Convergence testing

Convergence of GW-BSE calculations is a multi-step procedure. The GW part of the calculation is the critical one, so generally convergence can focus on the GW part. For 2D-systems, though, the BSE calculation exhibits a strong dependence on the k-grid employed.

Therefore, this convergence study is laid out as follows:

1. Simplified GW calculation
  - a. Screened cutoff (number of G-vectors) and the number of bands are converged together
  - b. The number of frequency grid points is converged using the obtained screened cutoff and number of bands from step a)
2. Full BSE calculation
  - a. Convergence with the k grid is tested

#### 1. Simplified GW calculation

The simplifications consist of full use of symmetry, omitting spin-orbit coupling, and using a coarse k grid of 6x6x1. The convergence with respect to the k grid is independent from the other parameters, therefore we could choose an economical k grid here.

In step 1a) we first tested the dependence of the quasiparticle bandgap on the screened cutoff, keeping the number of bands and the number of frequency grid points at very high values (VASP tags: NBANDS=1000 and NOMEGA=256, respectively). In VASP, the screened cutoff is by default set to two-thirds of the plane wave cutoff (VASP tags: ENCUTGW=ENCUT\*2/3).

The results are seen in Figure S1 a). At a plane wave cutoff of 550 eV (screened cutoff of 367 eV) and higher, the band gap at K varies only by less than 1 meV. At 400 eV, the value chosen for the main calculations of this paper, the band gap is converged within 3 meV.



Then, we tested the dependence of the quasiparticle bandgap on the number of bands (VASP tag: NBANDS), keeping the plane wave cutoff and the number of frequency grid points at very high values (VASP tags: ENCUT=700 and NOMEGA=256, respectively).

The results are seen in Figure S1 b). Employing 1024 bands, the band gap at K is 2.627 eV. For 640 bands, the value chosen for the main calculations of this paper, the band gap is 9 meV larger than for 1024 bands. It seems, that convergence is not yet reached at 1024 bands. From these tests we can estimate the band gap error of our main calculations to be in the range of 10s of meV.

In a subsequent step (1b), we employed a plane wave cutoff of 400 eV and set the number of bands to 640 (main calculation settings) to test the dependence of the band gap on the number of frequency grid points (VASP tag: NOMEGA).

The results are seen in Figure S2 a). For the band gap at K, we see a rapid decrease of the band gap with an increasing number of frequency grid points. Starting from 160 frequency grid points, the decrease slows down and changes happen at the meV scale, nearing convergence. Comparing the band gap at the highest number frequency grid points chosen here (256, band gap = 2.638 eV) with the value chosen for our main calculations (96, band gap = 2.70 eV), we overestimate the band gap by ca. 60 meV.

In summary, all three parameters taken together introduce an error of the band gap of less than 0.1 eV, which can be seen as the convergence goal for our purposes. Furthermore, the value of the band gap of 2.6 – 2.7 eV compares well with the benchmark of 2.67 eV established by Qiu et al.<sup>49</sup>. As a conclusion, our GW calculations can be regarded as a reliable basis for subsequent BSE calculations.

It should be noted that convergence tests were performed without taking the spin-orbit coupling into account. Results reported in the main text, however, included relativistic effects. We expect results of the convergence studies to be transferable.

## 2. Full GW-BSE calculation

In a final step, we used the full GW-BSE calculations as described in the main publication and tested the main conclusions of the spectral spacing of exciton energies at K on their k grid dependence. Here the spin-orbit coupling is included. The first main conclusion is that the spin-forbidden dark exciton at K is lower in energy than the bright exciton. This can be described by  $\Delta E_{\text{dark-bright}} < 0$ . The second main conclusion is that there exists an indirect exciton at K/K' that is even lower in energy than the direct dark

exciton at K. This can be described by  $\Delta E_{\text{dark-ind}} > 0$ . There are two different indirect excitons at K due to spin-orbit coupling: one is spin forbidden, the other spin-allowed. Therefore, we must distinguish between  $\Delta E_{\text{dark-ind\_spin-allowed}}$  and  $\Delta E_{\text{dark-ind\_spin-forbidden}}$ .

The results are seen in Figure S2 b). It is clearly seen that after exceeding a k grid of  $6 \times 6 \times 1$ ,  $\Delta E_{\text{dark-bright}}$  is always smaller than zero and  $\Delta E_{\text{dark-ind\_spin-allowed}}$  ( $\Delta E_{\text{dark-ind\_spin-forbidden}}$ ) is always negative (positive). Therefore, increasing the k grid does not change our main conclusions: the lowest-energy exciton is indirect at K/K' followed by the dark direct exciton at K. In fact, the differences of  $\Delta E$  at different k grids are small; they are below 2 meV in all cases.

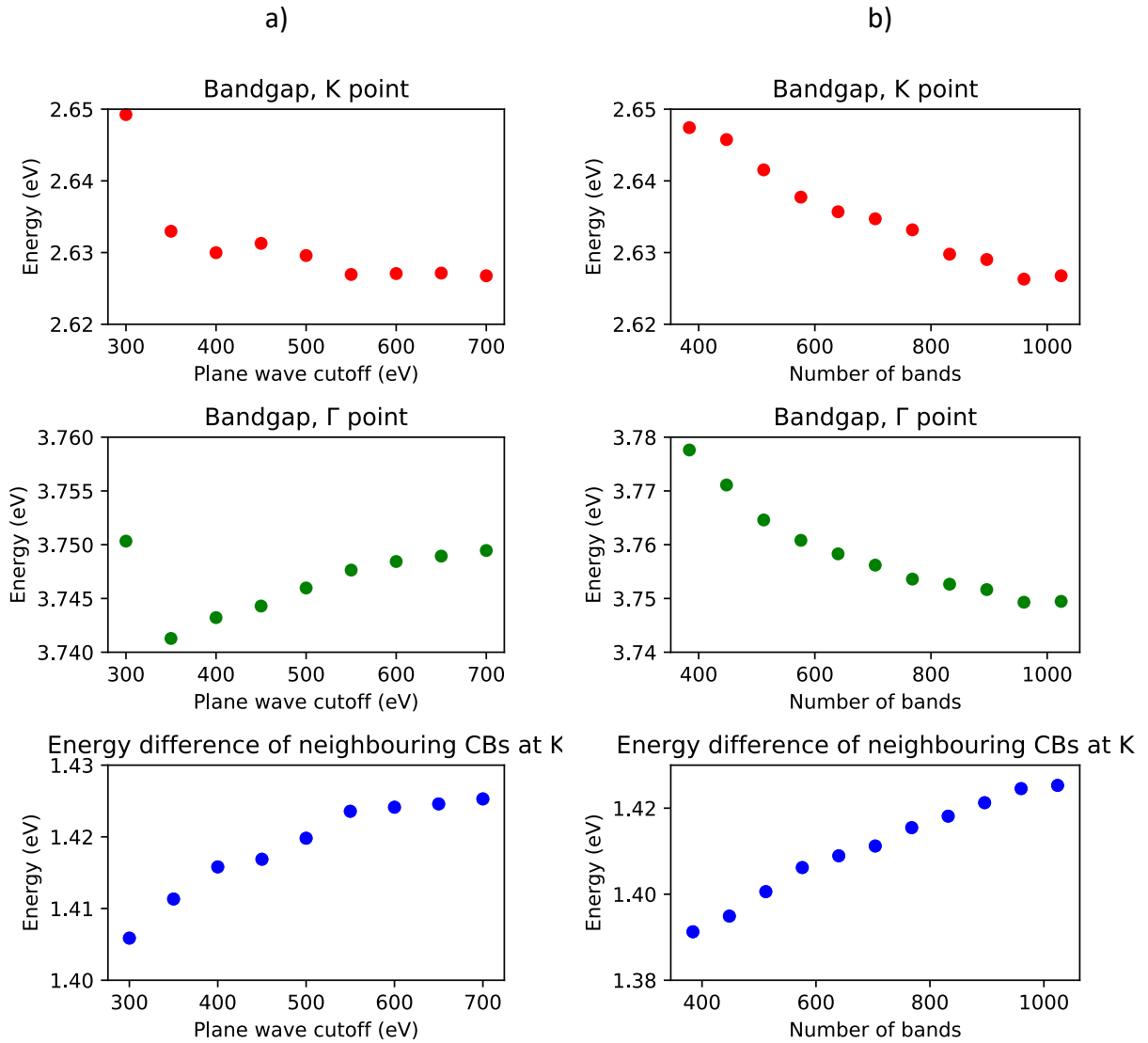


**Figure S1:** Convergence of the non-relativistic quasiparticle band gap with a) the screened cutoff (2/3 of the plane wave cutoff) and b) the number of bands. Shown are the bandgap at the K point, the gap at the  $\Gamma$  point and the difference between the two lowest-energy conduction bands. These convergence tests were performed for a simplified GW setup.

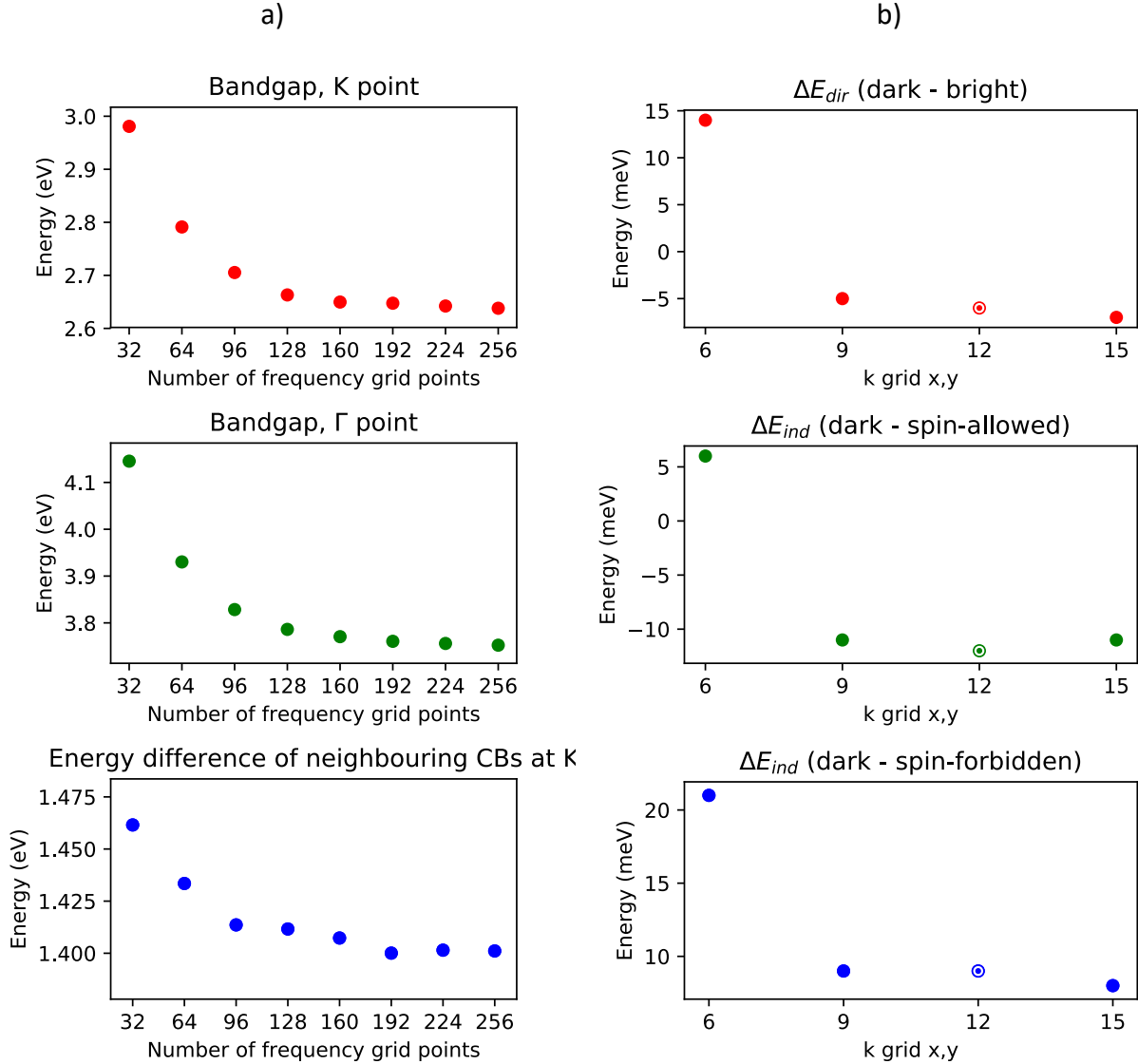


**Figure S2:** a) Convergence of the non-relativistic quasiparticle band gap with number of frequency grid points. Shown are the bandgap at the K point, the gap at the  $\Gamma$  point and the differenced between the two lowest-energy conduction bands. These convergence tests were performed for a simplified GW setup. b) Convergence of the spectral spacing of the main excitons at the K point with k grid. Shown are the energy difference between the direct bright and dark excitons at K, the energy difference between the dark direct exciton at K and the indirect spin-allowed exciton at K/K', as well as the energy difference between the dark direct exciton at K and the indirect spin-forbidden exciton at K/K'. The white circles indicate results for a calculation employing the Tamm-Dancoff approximation; the results are identical with the full BSE results.

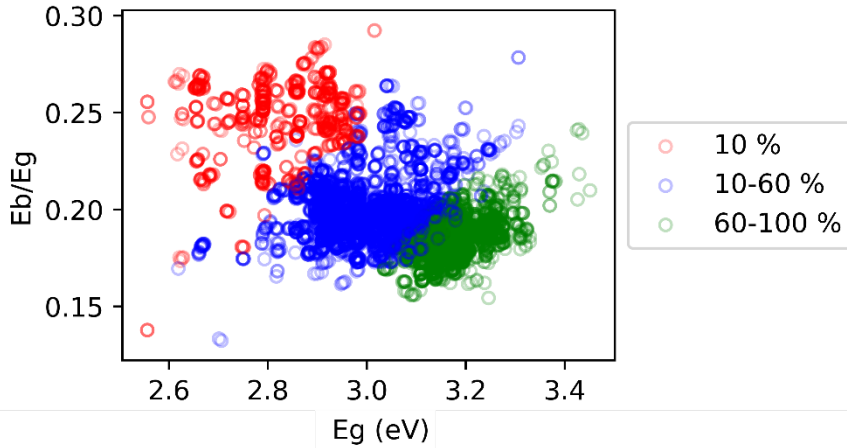


**Figure S3:** Change of the  $E_b/E_g$  ratio with  $E_g$ .  $E_b$  denotes the exciton binding energy and  $E_g$  the relativistic quasiparticle band gap energy. The color-coding marks reflect the percentage of lowest-energy excitons from the total of 100 excitons for each eigenstate (lowest-energy 10 % = red etc.). As a general trend, the  $E_b/E_g$  ratio decreases as the quasiparticle energy increases. This is due to screening of lower-energy excitons. This decrease explains why higher-energy excitons do not follow the  $E_b/E_g=0.25$  rule.

**Table S1:** Dependence of the exciton binding energy on the  $k$  grid density. Here the exciton binding energy of the lowest-energy direct exciton at the K point is shown.

$k$ grid	Exciton binding energy (eV)
15 x 15 x 1	0.551
12 x 12 x 1	0.637
9 x 9 x 1	0.790
6 x 6 x 1	1.061